PROCEEDINGS A

rspa.royalsocietypublishing.org

Research

Cite this article: Gilmore CK, Barrett SRH. 2015 Electrohydrodynamic thrust density using positive corona-induced ionic winds for in-atmosphere propulsion. *Proc. R. Soc. A* **471**: 20140912.
http://dx.doi.org/10.1098/rspa.2014.0912

Received: 23 November 2014
Accepted: 14 January 2015

Subject Areas:
plasma physics, electromagnetism, fluid mechanics

Keywords:
electrohydrodynamics, ionized gases, thrust density

Author for correspondence:
Steven R. H. Barrett
e-mail: sbarrett@mit.edu

Electronic supplementary material is available at http://dx.doi.org/10.1098/rspa.2014.0912 or via http://rspa.royalsocietypublishing.org.

Electrohydrodynamic thrust density using positive corona-induced ionic winds for in-atmosphere propulsion

Christopher K. Gilmore and Steven R. H. Barrett

Laboratory for Aviation and the Environment, Department of Aeronautics and Astronautics, Massachusetts Institute of Technology, 77 Massachusetts Avenue, Cambridge, MA 02139, USA

Previous work has characterized electrohydrodynamic (EHD) thruster performance, determining that thrust-to-power ratios are comparable with that of conventional propulsion at the laboratory scale. Achievable thrust density of EHD propulsion has yet to be experimentally quantified and could be a limiting factor in its application. In this paper, we quantify the achievable thrust density for a wire-to-cylinder electrode geometry using positive corona discharges for electrode pairs operating in parallel and in series. Geometric parameters, including the non-dimensional inter-pair and stage spacings, are varied, and the effect on current and thrust is measured. We estimate a maximum thrust per unit area of $3.3\,\mathrm{N\,m^{-2}}$ and a maximum thrust per unit volume of $15\,\mathrm{N\,m^{-3}}$, which we compare with the characteristic thrust density of a range of aircraft. We find that trade-offs exist between thrust density and the achieved thrust-to-power ratio, where increases in the former through either increased power input or pair packing density lead to decreases in the latter. We conclude that EHD propulsion has the potential to be viable from both an energy efficiency perspective (our previous study) and a thrust density perspective (this paper), with the greatest likelihood of viability for smaller aircraft such as unmanned aerial vehicles.

1. Introduction

Electrohydrodynamic (EHD) propulsion provides thrust through the coupling between electrostatic body forces and a neutral fluid, such as air. Ions generated in the neutral fluid and under the influence of an applied

THE ROYAL SOCIETY PUBLISHING

electric field collide with neutral fluid molecules, generating what is known as an electric or ionic wind [1]. The resulting force on the electrodes used to sustain the electric field generates a net thrust opposite to the direction of ion flow, and does so without moving parts or direct gaseous emissions.

Concepts associated with ionic winds have been applied to several different research areas including heat-transfer enhancement [2–4], particulate removal [5,6], electro-spinning/spraying [7,8] and ion drag pumping [9–11]. This has also motivated literature focused on developing computational models to solve the EHD governing equations [12–17]. In aerospace engineering, research efforts have focused on using dielectric barrier discharges (DBDs) to provide aerodynamic flow control to prevent subsonic boundary layer separation over aerofoils [18–20]. However, few studies in the literature have assessed the use of ionic winds in propulsion applications.

Generation of an ionic wind requires ionization of air at atmospheric pressure and temperature, the corona discharge [21] being a commonly applied method. A corona discharge requires the application of a potential difference across a pair of asymmetrical electrodes. At a sufficiently high potential difference, termed the corona inception voltage, an electric field of sufficient strength at the electrode with the smaller radius of curvature (the emitter) is induced such that ionization can take place. The ions then travel from the emitter under the influence of the electric field to the electrode of larger radius (the collector). The speed at which the ions travel is determined by the local electric field and ion mobility, the latter a measure of resistance owing to collisions experienced by an ion travelling through a particular medium. Using direct current voltage sources, either a positive or a negative corona discharge is induced owing to a positive or negative emitter polarity relative to the collector [21]. We note that other ionization methods exist for atmospheric pressure and temperature, such as DBD, but we consider only the positive corona discharge in this paper.

Christensen & Moller [22] published the first peer-reviewed experimental analysis of EHD propulsion in 1967, where they concluded that ion mobility was an important factor in determining thrust. Previous work performed by Masuyama & Barrett [23] quantified EHD thruster performance. Specifically, they determined that achievable thrust-to-power ratios (also referred to as thrust effectiveness [22]) of EHD propulsion were on the order of 5–10 $\mathrm{N\,kW^{-1}}$, with measured ratios reaching 100 $\mathrm{N\,kW^{-1}}$ compared with approximately 2 $\mathrm{N\,kW^{-1}}$ on average for jet propulsion [24]. Thrust-to-power ratio was found to be dependent on both applied potential difference and the distance between the emitter and collector, which we refer to as the electrode gap distance. These ratios were achieved at the laboratory scale where distances between electrodes were on the order of centimetres, and power output was on the order of watts. In addition, thrust-to-power ratios on the order of 100 $\mathrm{N\,kW^{-1}}$ were achieved shortly after corona inception when the total generated thrust was on the order of approximately 1 mN. Independent experimental efforts subsequently published (but likely carried out in a similar time frame) by Moreau *et al.* [25] and Kiousis *et al.* [26] broadly confirm these findings.

Masuyama & Barrett [23] and Colas *et al.* [27] also studied dual-stage thrusters, consisting of separate ionizing and accelerating regions generated by an intermediate potential electrode. Masuyama & Barrett [23] observed increases in thrust-to-power ratio, and Colas *et al.* [27] noted higher maximum achievable thrusts relative to the single-stage configurations. Finally, Saenz-Otero *et al.* [28] designed and tested an EHD thruster device at zero-gravity using pin-to-mesh geometries as a proof of concept study for a potential propulsion mechanism for robotic assistants operating in, for example, a space station. Sensitivity studies were performed with regard to pin packing density, but thrust density was not quantified.

Numerical investigations performed by Zhao & Adamiak [12] as well as Martins & Pinheiro [13] calculated thrust for a two-dimensional EHD device. Both studies modelled a configuration similar to that of the 'lifter' concept, with Martins & Pinheiro [13] concluding that the thrust is electrostatic in origin and is concentrated on the collecting electrode. Another numerical analysis by Martins & Pinheiro [14] quantified the sensitivity of thrust output with respect to collecting electrode diameter, determining that thrust increased with diameter owing to higher levels of

ionization at the emitting electrode. A further numerical analysis performed by Martins [15] considered an improved thruster design with multiple collecting stages for a single emitting electrode. The thrust achieved in these numerical analyses is on the same order of magnitude as the thrusts observed in Masuyama & Barrett [23] and Moreau *et al.* [25], although the level of agreement was dependent on modelling assumptions such as emitter boundary conditions. Indirect boundary conditions used to set the amount of ionization (charge injection) at the emitting electrode, such as Kaptsov's hypothesis [29], have been used or have been the subject of other numerical studies [30,31].

While the achieved thrust-to-power ratios found by EHD are comparable with conventional propulsion, Masuyama & Barrett [23] identified the achievable thrust density as the next potential limitation—a topic that to our knowledge that has not been experimentally or numerically addressed in the literature. As electrode pairs are brought together in the attempt to increase thrust density, the electric fields generated by each pair are expected to interact such that the current and thrust characteristics of the system are affected. The purpose of this work is to quantify the achievable thrust density at the laboratory scale for a similar experimental set-up and electrode geometry used in Masuyama & Barrett [23]. We consider the thrust density achieved by both parallel and series operation of electrode pairs. Parallel operation refers to configurations in which all emitters lie in one plane and all collectors lie in another, where these two planes are parallel to each other. This can also be thought of as pairs operating side by side. Series operation refers to configurations in which the emitters and collectors all lie in the same plane and can be thought of as pairs operating end to end. Series operation has also been referred to as 'staging' in the literature, a term which is used also in this paper. A one-dimensional (1D) analytical analysis performed by Stuetzer [9] considered both parallel and series ion drag pumps and determined the corresponding impact on pump performance. No interaction between stages was assumed. Experimental investigations of operating multiple EHD devices in series, or staging, have been performed with focus placed indirectly on thrust generation by attempting to maximize ionic wind velocity [32–34], finding that staging allowed for higher achieved fluid velocities. However, extensions to achievable thrust density were not made.

Our work is divided into three components:

I. an analysis of interactions between two electrode pairs in parallel;
II. a study of thrust arrays (i.e. parallel operation of multiple electrode pairs); and
III. an investigation of thrust staging (for parallel and series operation).

Component I examines the dependence of current and thrust produced from a positive corona-induced ionic wind on certain geometric parameters, in particular the spacing between electrode pairs operating in parallel. Component II aims to quantify the achievable thrust density for a selected electrode geometry when considering multiple parallel electrode pairs. Finally, component III aims to quantify the achievable thrust per unit volume when multiple electrode pair stages are considered, building upon the results from components I and II. Results from these three components are presented in §§4, 5 and 6, respectively. In addition, §2 provides some theoretical insights and fundamental limitations of EHD thrust to help motivate the discussion of results. In particular, we extend previous derivations for the maximum thrust per unit area of electrostatic thrusters to include characteristics of the corona discharge.

2. Theory

This section provides a brief overview of the 1D theory previously derived in Masuyama & Barrett [23] as well as providing a general extension when considering space charge effects. In addition, a theoretical limit on achievable thrust density for EHD propulsion is derived. Finally, we show that the thrust-to-power ratio of an EHD system is independent of the electric field shape for a given electrode gap distance when dimensionality effects are considered.

(a) Generalization of thrust-to-power expression to include space charge effects

As was previously derived in Masuyama & Barrett [23], 1D theory states that EHD thrust is equal to the magnitude of the Coulomb force on the injected ions persisting in a gap between two electrodes, which was shown to be

$$T = \frac{IL}{\mu}, \tag{2.1}$$

where I is the current generated by the thruster, L is the distance between the emitter and collector and μ is the ion mobility. Equation (2.1) was derived assuming parallel plate electrodes (i.e. 1D geometry) and negligible space charge effects. The thrust-to-power ratio, T/P, in 1D is [23]

$$\frac{T}{P} = \frac{L}{\mu \Delta V}, \tag{2.2}$$

where ΔV is the applied potential difference. Although space charge effects are small just after corona inception, this may not be the case at higher induced currents. Here we show that even with the inclusion of space charge effects, thrust is still determined by equation (2.1), and T/P is still determined by equation (2.2) in 1D. In the absence of drag, thrust per unit area of the electrode is equal to the integration of the Coulomb force over the domain, or in 1D

$$\frac{T}{A} = \int_0^L \rho E \, \mathrm{d}x, \tag{2.3}$$

where ρ is the space charge concentration, E is the electric field magnitude and x is the coordinate between the electrodes defined such that $x = 0$ at the emitter and $x = L$ at the collector. In the absence of magnetic fields and time varying electric fields and assuming a steady system, Gauss's law and the steady law of current conservation apply, where the latter, in differential form, is

$$\nabla \cdot \boldsymbol{j} = \nabla \cdot [\rho(\mu \boldsymbol{E} + \boldsymbol{u})] = 0, \tag{2.4}$$

where $\boldsymbol{j}$ is the current density (current per unit area) and $\boldsymbol{u}$ is the neutral fluid velocity. $\rho\mu\boldsymbol{E}$ is known as the drift current and $\rho\boldsymbol{u}$ the convective current. A common modelling assumption is to neglect the neutral fluid velocity relative to the ion drift velocity, $\mu\boldsymbol{E}$ [12–14]. Ionic wind velocities at the laboratory scale have been reported to be between 1 and 10 $\mathrm{m\,s^{-1}}$ [25]. Assuming an ion mobility of 2×10^{-4} $\mathrm{m^2\,V^{-1}\,s^{-1}}$ [35] and an average electric field strength of 5×10^5 $\mathrm{V\,m^{-1}}$, the drifty velocity is on the order of 100 $\mathrm{m\,s^{-1}}$, meaning that the induced neutral fluid velocity is approximately 1–10% of the drift velocity. Making this assumption and simplifying to 1D reduces equation (2.4) to

$$\frac{\mathrm{d}j}{\mathrm{d}x} = \frac{\mathrm{d}}{\mathrm{d}x}(\rho\mu E) = 0. \tag{2.5}$$

Assuming that ion mobility is constant, equation (2.5) implies that ρE is invariant along the electrode gap. Taking the space charge concentration and electric field magnitude at the emitting electrode, equation (2.3) reduces to

$$T = \rho|_{x=0}\, E|_{x=0}\, LA = \frac{jLA}{\mu} = \frac{IL}{\mu},$$

yielding the same result as in equation (2.1). Given that the power consumed by the electrodes is the applied potential difference, ΔV, multiplied by the current, I, the thrust-to-power ratio is identical to equation (2.2). This result indicates that regardless of the effect of space charge on the electric field under the given assumptions and a chosen electrode gap distance, thrust is directly proportional to current and electrode gap distance and inversely proportional to ion mobility. These results also extend to both parallel and series operation of 1D electrode pairs. Parallel operation is equivalent to increasing the electrode area, which proportionally increases thrust according to equation (2.3). Series operation is equivalent to multiple stages of emitter and collector plates, where if no interaction is assumed between stages and each pair has the same electrode area, gap distance and applied potential difference, equation (2.1) scales with the number of stages.

(b) Theoretical limit on thrust density

While we have established that thrust is proportional to the generated current regardless of space charge effects, there exists a fundamental limitation on the amount of current an EHD thruster or device can generate, similar to the limitations associated with electrostatic thrusters used in space propulsion applications [36]. We consider a 1D electrode geometry. Beginning with Gauss's law and the steady current conservation law in 1D, again making the approximation that the neutral fluid velocity is negligible relative to the drift velocity, it can be shown that the applied potential across the electrodes, V_a, is equal to

$$V_\mathrm{a} = \left[\left(\frac{\mu\epsilon E_0^2}{3j} + \frac{2L}{3}\right)\left(E_0^2 + \frac{2jL}{\mu\epsilon}\right)^{0.5}\right] + \frac{\mu\epsilon E_0^2}{3j}, \tag{2.6}$$

where E_0 is the electric field magnitude at the emitter. Equation (2.6) can then be solved for the current density, j, as a function of E_0, L and V_a. The magnitude of the electric field at the emitter, E_0, needs to be prescribed as a boundary condition. Pekker & Young [37] assume that the solution is choked, i.e. $E_0 = 0$. Solving equation (2.6) for the choked condition yields the Mott–Gurney law [38], or

$$j_\mathrm{MG} = \frac{9}{8}\mu\epsilon\frac{V_\mathrm{a}^2}{L^3}, \tag{2.7}$$

which sets the maximum current that can be passed between the two parallel plate electrodes. The choked solution is not applicable in the case of corona discharges as a critical electric field magnitude, E_i, at the emitting electrode is required such that charge injection can take place [21]. This specifies a corona inception voltage, V_i, which must be applied before current and thrust are generated by the electrodes. Here, we extend the Mott–Gurney law to account for the corona inception voltage and determine the corresponding impact on maximum theoretical thrust output. Empirical relations for inception voltages for specific electrode geometries were originally developed by Peek [39]. For the 1D case, we combine the concept of an inception voltage with Kaptsov's hypothesis [29], which states that the electric field at the emitting electrode is equal to the value taken at corona inception for $V_\mathrm{a} \geq V_\mathrm{i}$, such that boundary condition for E_0 is

$$E_0 = E_i = \frac{V_\mathrm{i}}{L}, \tag{2.8}$$

where the final equality is given by the magnitude of the electric field in the absence of space charge between parallel plate electrodes. Zahn *et al.* [40] performed a survey of different boundary conditions for a steady and transient analysis for a similar problem. We also further specify that the corona inception voltage is some fraction of the applied potential difference across the electrodes, or

$$V_\mathrm{i} = \alpha V_\mathrm{a}. \tag{2.9}$$

Combining equations (2.6)–(2.9), the ratio between the current density for $E_0 > 0$ and the choked solution is solved for. This ratio, which we denote by λ, monotonically decreases from 1 to 0 as α varies from 0 to 1, with $\alpha = 0$ corresponding to the choked solution and $\alpha = 1$ corresponding to the case where no charge injection has taken place. The theoretical maximum thrust density for a 1D EHD propulsion device is then given by

$$\frac{T}{A} = \begin{cases} 0 & V_\mathrm{a} \leq V_\mathrm{i} \\ \dfrac{9}{8}\epsilon\lambda\dfrac{V_\mathrm{a}^2}{L^2} & V_\mathrm{a} > V_\mathrm{i} \end{cases}, \tag{2.10}$$

where accounting for an inception voltage has decreased the theoretical maximum thrust density relative to the choked solution predicted by equation (2.7). Several observations can be made of equation (2.10). First, there is no dependence on ion mobility. Second, the thrust per unit volume will monotonically decrease for a given V_a as L increases. Third, if V_a/L, or the average electric field magnitude, remains constant as the thruster geometry is scaled, this would result in

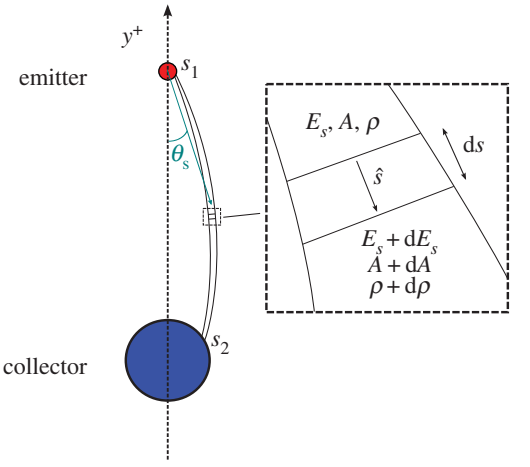

Figure 1. Current-tube illustration for a two-dimensional wire-to-cylinder geometry. (Online version in colour.)

a constant maximum achievable thrust per unit area regardless of the size of the thruster. Thrust per unit volume would also be monotonically decreasing with increasing electrode gap distance when dividing equation (2.10) by L. Detailed derivations of equations (2.6) and (2.10) are provided in the electronic supplementary material.

(c) Proof that thrust-to-power ratio is not a function of E-field shape

While it is expected that the electric fields of electrode pairs will interact with increased electrode packing density, it is unknown what effect these interactions will have on the system thrust-to-power ratio. In Masuyama & Barrett [23], it was found that the 1D thrust-to-power equation given by equation (2.2) predicted the trend of thrust-to-power ratio as a function of generated thrust qualitatively, i.e. thrust-to-power ratio decreased with increasing power input, but under-predicted thrust-to-power ratio at larger values of L. Given that increases in L corresponded to decreasing the ratio between the length of the emitting wire to the gap distance, it was hypothesized that dimensionality effects could be an explanation for the deviation from 1D theory. Understanding the effect of altering electric field shape on thrust-to-power ratio may give insight into possible trade-offs with increasing thrust density given the anticipated interactions between electrode pairs and the extent to which thrust-to-power ratio can be engineered by geometric changes.

To understand this dependence we return to equation (2.4), again neglecting the bulk fluid velocity, and apply it to a generic 'current tube'—a concept that was also applied in the analysis performed by Sigmond [41]. [A 'current tube' is analogous to a streamtube in which charge (fluid) is flowing under the effect of an electric field (pressure gradient).] The boundaries of the current tube are determined by the electric field lines when only the drift current is considered, as has been derived previously, for example, by Davis & Hoburg [17]. An example of a current tube is shown in figure 1 for a two-dimensional wire-to-cylinder geometry.

By considering a differential element in the current tube, as depicted in the dashed box in figure 1, we see that there are perturbations $\mathrm{d}E_s$, $\mathrm{d}\rho$ and $\mathrm{d}A$ to the electric field along the current tube, E_s; charge density, ρ and current-tube area, A, respectively. Applying current conservation across this differential element, we see that

$$\mu\left[-\rho E_s A + (\rho + \mathrm{d}\rho)(E_s + \mathrm{d}E_s)(A + \mathrm{d}A)\right] = \mathrm{d}(\rho E_s A) = 0, \tag{2.11}$$

or that the quantity $\rho E_s A$ is invariant along the current tube, a result similar to that in equation (2.5). The Coulomb force on that differential element is

$$\mathrm{d}\boldsymbol{F} = \rho \boldsymbol{E} A\, \mathrm{d}s, \tag{2.12}$$

where ds is the length of the element and $\boldsymbol{E} = E_s\hat{s}$ as dictated by the current-tube definition, with $\hat{s}$ being the unit vector along the current tube, as shown in figure 1. Using Cartesian coordinates and taking the direction of thrust to be in the positive y-direction, the thrust contribution of the differential element is the scalar product between the negative of equation (2.12) (as the thrust is the reaction to the Coulomb force) and the direction of thrust, or

$$\mathrm{d}T = \mathrm{d}\boldsymbol{F} \cdot \hat{y} = -\rho \boldsymbol{E} A \,\mathrm{d}s \cdot \hat{y} = -\rho A \,\mathrm{d}s(\boldsymbol{E} \cdot \hat{y}) = \rho E_y A \,\mathrm{d}s, \tag{2.13}$$

where $\hat{y}$ is the unit vector and E_y the magnitude of the electric field component in the y-direction. The thrust contribution for the current tube is then obtained by integrating equation (2.13) along its entire length, i.e.

$$T = \int_{s_1}^{s_2} \mathrm{d}T = \int_{s_1}^{s_2} \rho E_y A \,\mathrm{d}s, \tag{2.14}$$

where s_1 and s_2 denote the start (emitter) and end (collector) points of the current tube, respectively. Now we define a local current-tube angle, θ_s, by the Cartesian coordinate vector, $\boldsymbol{r}$, as shown in figure 1. Equation (2.14) is now written in terms of the total electric field magnitude along the current tube, E_s, and θ_s as

$$T = \int_{s_1}^{s_2} \rho E_s \cos\theta_s A \,\mathrm{d}s = (\rho E_s A)_{s_1} \int_{s_1}^{s_2} \cos\theta_s \,\mathrm{d}s, \tag{2.15}$$

where $\rho E_s A$ is known to be constant from equation (2.11) and is chosen to be evaluated at the emitter. Realizing that $\mathrm{d}y = \cos\theta_s \,\mathrm{d}s$ and applying the appropriate change in variable, equation (2.15) simplifies to

$$T = (\rho E_s A)|_{s_1} \int_{y_1}^{y_2} \mathrm{d}y = (\rho E_s A)|_{s_1} \,\Delta y = \frac{I_s \Delta y}{\mu}, \tag{2.16}$$

where I_s is the current generated by the current tube and Δy is the difference between the y-coordinates of the starting and endpoints. Δy will be referred to as the 'thrust-oriented gap distance'. The power consumed by the current tube is

$$P = \Delta V I_s = \Delta V \mu \,(\rho E_s A)|_{s_1}. \tag{2.17}$$

Equations (2.16) and (2.17) are then combined to yield the thrust-to-power ratio of the current tube, or

$$\frac{T}{P} = \frac{(\rho E_s A)|_{s_1} \,\Delta y}{\Delta V \mu \,(\rho E_s A)|_{s_1}} = \frac{\Delta y}{\mu \Delta V}. \tag{2.18}$$

Equation (2.18) shows that, under the specified assumptions, the thrust-to-power ratio of an arbitrary current tube in an EHD system is only a function of the thrust-oriented gap distance for a given ion mobility and applied potential difference, i.e. the thrust-to-power ratio is path independent for a given thrust-oriented distance travelled. The total thrust is determined by integrating over all current tubes, which can then be used to determine the system thrust-to-power ratio.

While equation (2.18) shows that for a given Δy the thrust-to-power ratio is not a function of the current-tube path, i.e. E-field shape, it does not imply independence from electrode geometry. Start and endpoints for a given current tube, and thus the thrust-oriented gap distance, will depend on the generated electric field and the space charge distribution, which in turn are a function of electrode pair geometry. However, if the variations in geometry are small relative to the overall thrust-oriented gap distance, it is implied that deviations from 1D theory will be small. The results of this analysis also indicate that regardless of the geometry of the induced electric field, the thrust-to-power ratio will not be impacted and is robust to modifications in electric field shape. This means that engineering the electric field shape does not change efficiency. We therefore do not anticipate interactions between electrode pairs to introduce losses in thrust effectiveness in our experimental analysis. This result also suggests that the deviation from 1D theory observed in Masuyama & Barrett [23] was not a result of dimensionality effects.

Finally, we note that this result is dependent on the assumption that the drift current dominates other sources of current. If, for example, the bulk fluid velocity is no longer negligible relative to the drift velocity, then the conservation of current argument across the differential element given in equation (2.11) would need to be modified accordingly. The quantity $\rho E_s A$ would then no longer be invariant and the characteristic of current-tube path independence may fail to hold. Such a situation may arise, for example if a free-stream velocity were to be introduced. Masuyama & Barrett [23] showed theoretically that thrust-to-power ratio would decrease with the superposition of a free-stream velocity in 1D.

3. Experimental set-up and methodology

The three experimental components of our study use a similar set-up. A PTFE frame is used to support a set of acrylic brackets, where each set consists of a top bracket to support the emitting electrodes and a bottom bracket to support the collecting electrodes. For the case of staging, multiple sets are used. The emitting electrode is either AWG32 or AWG40 (0.202 or 0.0799 mm diameter, respectively) tinned copper wire. The collecting electrode is a 6.35 mm diameter Al 6061 tube.

The selected electrode geometry is consistent with Masuyama & Barrett [23], including the smallest ASTM B 258 standard copper wire size commonly available (AWG40) and a factor of 2.5 increase (AWG32). (Our results show no effect of this change.) We note that the stiffness of wires larger than 0.2 mm inhibited accurate fabrication and thrust measurement, while a sufficiently large emitter will fail to result in corona inception. A smaller emitter diameter than 0.08 mm would introduce significant fabrication and robustness difficulties, though may be the subject of future work. The collecting electrode size is sufficiently large as to prevent corona inception at the collector. A 6.35 mm electrode according to Peek's law [21,39] has an inception voltage on the order of 70 kV for the gap distances considered here, which is larger than the potential differences applied in this analysis. The collector diameter is not varied. Given the high conductivity of copper, it is assumed that the discharge will be approximately uniform along the emitter. Care is taken to not introduce bends in the wire that may create higher localized electric fields, thus modifying the uniformity of the discharge and potentially leading to earlier onset of electrical arcing.

The brackets have been designed such that electrode pairs can be spaced at 10 mm increments. The PTFE frame also allows for 10 mm vertical increments, matching the set-up of Masuyama & Barrett [23], where the electrode gap distances for all pairs are varied simultaneously. This pair spacing increment is selected so that any non-dimensional spacing can take an approximately integer value. The increment is also large enough so that there is no physical interference between the collecting electrodes of each pair. The PTFE frame is designed such that the emitting electrodes have a length of 200 mm. The collecting electrodes have a length of 500 mm in order to reduce the end effects from sharp edges on the aluminium tubing. As positive coronas are not directly dependent on ionization processes at the cathode [21], cathode surface conditions are not expected to affect discharge properties.

The experimental quantities of interest are voltage, current and thrust. Electrical power is provided by a Matsusada AU120P2.5 positive polarity power supply, which provides potential differences of up to +120 kV and up to 2.5 mA of current. The collecting electrodes are grounded in all experiments. Voltage and current are controlled and measured using a set of Matsusada high voltage digital controllers. Thrust is measured using an Ohaus ScoutPro scale and is calculated as a reduction in weight. A PVC frame supports the scale from which the PTFE frame is suspended. The PVC frame also serves the secondary purpose of isolating the PTFE frame and electrode pairs from the surroundings in an attempt to limit extraneous induced currents as well as to simulate thruster operation in an open environment. The scale has a 0.6 kgf limit while providing thrust measurements at ±0.01 gf (approx. 0.1 mN) resolution. Applied voltages were varied at approximately 1 kV increments where 20 voltage, current and thrust data points are taken at each increment.

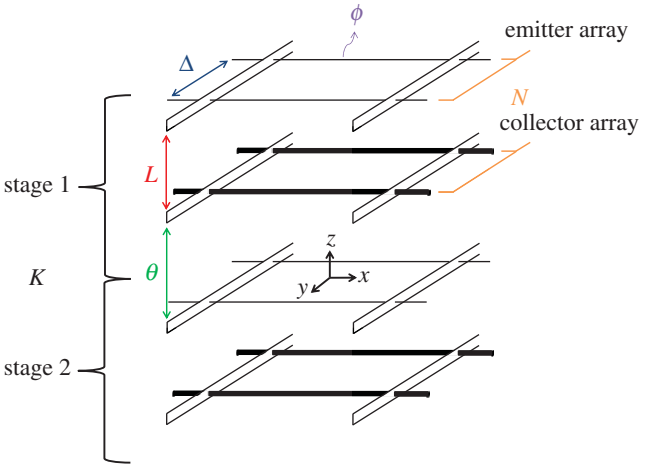

Figure 2. Illustration of the emitter and collector arrays with associated geometric parameters varied in this study. L is the electrode gap distance, Δ is the electrode pair spacing, θ is the distance between electrode pair stages, ϕ is the emitting electrode wire diameter, N is the number of electrode pairs per stage and K is the number of stages. The area used in calculating thrust per unit area is defined in the x—y plane. All references to 'area' in this paper refer to this orientation. Thrust on the arrays is produced in the positive z-direction, with the induced fluid motion in the negative z-direction. (Online version in colour.)

The following subsections describe each component in greater detail.

(a) Component I: electrode pair interaction

The purpose of this component is to confirm the existence of electrode pair interactions as well as to understand and quantify the interaction between wire-to-cylinder electrode pairs as they are brought closer together during parallel operation. The number of electrode pairs, N, is limited to 2. When considering parallel operation, three geometric parameters are varied: (i) the electrode gap distance, L; (ii) the electrode pair spacing, Δ and (iii) the emitter wire diameter, ϕ. The number of stages, K, is fixed at 1. Note that the electrode gap distance, L, is defined between the two closest points of the emitter and collector. Figure 2 provides an illustration of the defined parameters for all three components of this study. The specific objectives for this component are to determine (i) how current and thrust are affected at a given applied voltage as Δ is decreased and the corresponding dependencies on Δ, L and ϕ, and (ii) how thrust scales with current for different values of Δ.

(b) Component II: thrust array

The purpose of this component is to quantify the achievable thrust density of our selected electrode geometry for parallel operation, i.e. $K = 1$, but N is no longer limited to 2. Up to $N = 5$ electrode pairs are tested. Two electrode gap distances ($L = 30$ and 50 mm) are considered, ϕ is not varied (AWG32), and Δ is varied from 10 mm to $L + 10$ mm. The specific objectives for this component are to determine (i) how current and thrust scale with the number of electrode pairs as a function of Δ; (ii) the achievable thrust density (both thrust per unit area and per unit volume) for electrode pairs operating in parallel; and (iii) the Δ at which thrust density is maximized for a given L. Note that the area used in calculating thrust per unit area is defined in the $x - y$ plane as shown in figure 2. This is a 'frontal area', i.e. the area perpendicular to the thrust direction. All references to 'area' in this paper refer to this orientation. Volume is determined by extruding the area in the z-direction.

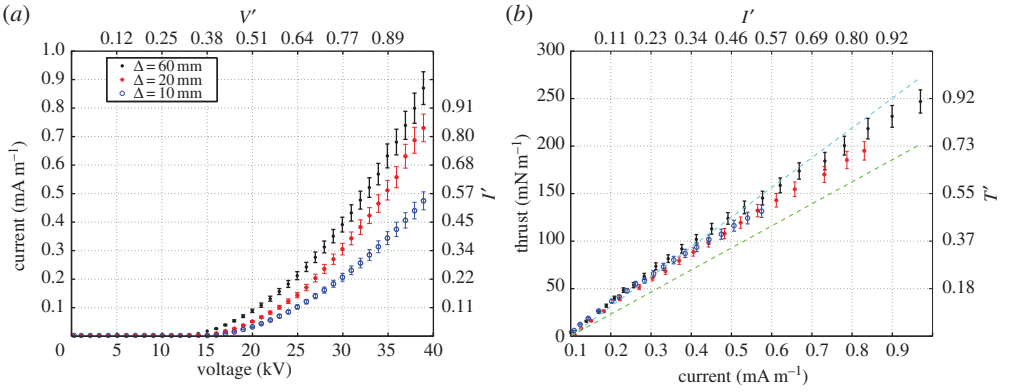

Figure 3. Experimental data collected for the case of $L = 50$ mm, where all dimensional results are plotted on a per unit length of emitting electrode basis: (*a*) current (mA m^{-1}) versus voltage (kV) and (*b*) thrust (mN m^{-1}) versus current (mA m^{-1}). 95% uncertainty intervals are shown for current in (*a*) and thrust in (*b*). (Online version in colour.)

(c) Component III: thrust staging

The purpose of this component is to quantify the achievable thrust density when electrode pair arrays have been linearly staged, i.e. the electrode pairs are operating both in parallel and in series. In this part, two stages ($K = 2$) are considered owing to the weight limit of the scale. First, the distance between the two stages, θ, is varied for a fixed Δ and L. $N = 2$ and $\Delta/L = 2$ for each stage. Second, the thrust density is estimated, as will be described in §6. ϕ is not varied (AWG32). The specific objectives for this component are (i) to determine how current and thrust scale with the number of stages at a given inter-stage gap, θ, and the dependence of this scaling on θ and L; (ii) to estimate the achievable thrust density for electrodes operating both in series and in parallel; and (iii) to determine the θ at which thrust density is maximized for a given L and Δ.

(d) Experimental uncertainty

An additional set of experiments is conducted in order to quantify experimental uncertainty in the measurements of thrust, current and voltage. This is done by performing a series of voltage sweeps for the same electrode configuration without modification or manipulation as well as by deconstructing and reconstructing a given configuration between each sweep to account for fabrication and other experimental procedure-related uncertainty and variability. Similar variability in thrust is observed in both sets of tests, but higher variability in current is observed in the latter. Based on this analysis, estimated uncertainties at 95% confidence are approximately ±5%, ±5% and ±0.01% for thrust, current and voltage, respectively, at voltages near the spark breakdown threshold. This variability is also, in general, larger than the variability observed in the 20-point time-series data taken at each voltage (approx. 2%), although is on the same order of magnitude. However, given that estimated relative uncertainties are small and on the order of 5%, this indicates repeatability in experimental outcomes. In the results presented in §§4, 5 and 6, standards for measurement uncertainty as outlined by Coleman & Steele [42] are applied.

4. Component I results: electrode pair interaction

Figure 3 is an example of the experimental data collected for an electrode gap distance $L = 50$ mm and electrode pair spacings $\Delta = 10$, 20 and 60 mm. Dimensional thrust and current data are normalized by the emitting electrode length. Non-dimensional current and voltage (I', V') are defined as

$$X' = \frac{X}{X_{b,\Delta_{60}}},$$

where X is current or voltage and $X_{b,\Delta_{60}}$ is the corresponding value at the highest voltage tested for $\Delta = 60$ mm. Data are normalized to $\Delta = 60$ mm as it will be shown in §4*a* that electrode pair interactions become important when the pair spacing is equal to or less than the electrode gap distance. For the plotted data in figure 3, the highest voltage tested is 39 kV as spark breakdown, i.e. electrical arcing, occurred at or near 39–40 kV. Non-dimensional thrust is defined as

$$T' = T\frac{\mu}{I_{b,\Delta_{60}}L},$$

or the thrust for a given pair spacing normalized by the theoretical thrust from equation (2.1) for an assumed ion mobility. Non-dimensional thrust-to-power ratio is defined as

$$\frac{T}{P'} = \frac{T}{P}\cdot\frac{\mu V_{b,\Delta_{60}}}{L},$$

where the thrust-to-power ratio of a given configuration is normalized by the theoretical value given by equation (2.2) for an assumed mobility. For non-dimensional thrust and thrust-to-power ratio, the mobility is assumed to be that of saturated air, which is given below.

From figure 3*a*, as Δ decreases, the current induced at a given voltage also decreases, confirming the existence of electrode pair interactions, where the $\Delta = 10$ mm case achieves 55% of the current at spark breakdown when $\Delta = 60$ mm. Figure 3*b* shows that the thrust generated at a given induced current is approximately independent of Δ, i.e. the implied mobility linearly relating thrust to current, given by equation (2.1), is not affected by electrode pair interactions up to approximately 0.30 mA m^{-1} ($I' = 0.34$).

The average implied mobility from the results presented in figure 3*b* ranges from 1.554 to 1.670×10^{-4} m^2 V^{-1} s^{-1}, as determined by a linear regression of the data, where the relative humidity (RH) at the time of data collection was approximately 50%. Ion mobility has been shown to decrease with increasing water vapour content, arising from ion clustering as proposed by Ryzko [43]. Thus for a given current, more thrust is predicted for a thruster operating in humid as opposed to dry air. Theoretical thrust versus current curves as determined by equation (2.1) are provided for reference using ion mobilities for dry and saturated (100% RH) air, 2.155×10^{-4} m^2 V^{-1} s^{-1} and 1.598×10^{-4} m^2 V^{-1} s^{-1}, respectively [35], and are given by the green and cyan dashed lines. We note that Moreau *et al.* [25] determined ion mobilities on the order of 3.0×10^{-4} m^2 V^{-1} s^{-1}, approximately 1.8–1.9 times higher than those observed for this particular dataset.

In figure 3*b*, deviation from theory where thrust is no longer linear in current is thought to be due to bilinear performance degradation, as proposed by Masuyama & Barrett [23]. At these higher currents, it was hypothesized that reverse current flow was induced owing to a discharge at the ground electrode, causing an increase in current but a decrease in thrust given the opposing ion flow. This hypothesis has yet to be experimentally confirmed. Similar performance degradation is observed in figure 3*b*; thrust versus current curves for $\Delta = 20$ mm and 10 mm track approximately with the low mobility theoretical curve (cyan) up to $I' = 0.34$, after which thrust deviates from linearity. Notable performance degradation for $\Delta = 60$ mm occurs at approximately $I' = 0.69$, where at breakdown $T' = 0.92$.

Figure 4 gives thrust-to-power ratio as a function of (i) applied voltage and (ii) thrust. Theoretical thrust-to-power curves as determined by equation (2.2) using dry and saturated air ion mobilities are provided for reference in figure 4*a*. We find the same relation between T/P and thrust in figure 4*b* as observed in Masuyama & Barrett [23], where thrust-to-power ratio decreases with increasing power and thrust and T/P' falling below 1 at spark breakdown for each Δ. Figure 4*a* shows that the experimental results, regardless of electrode pair spacing, are consistent with 1D theory, where the three plotted datasets converge towards a single curve bounded by the theoretical curves as voltage is increased. Figure 4*a* also supports the conclusion from §2c that thrust-to-power ratio is approximately independent of electric field shape as interactions between pairs are expected to distort the electric field shape. We qualify the previous statement as 'approximately independent' given that thrust-to-power is dependent on electrode geometry,

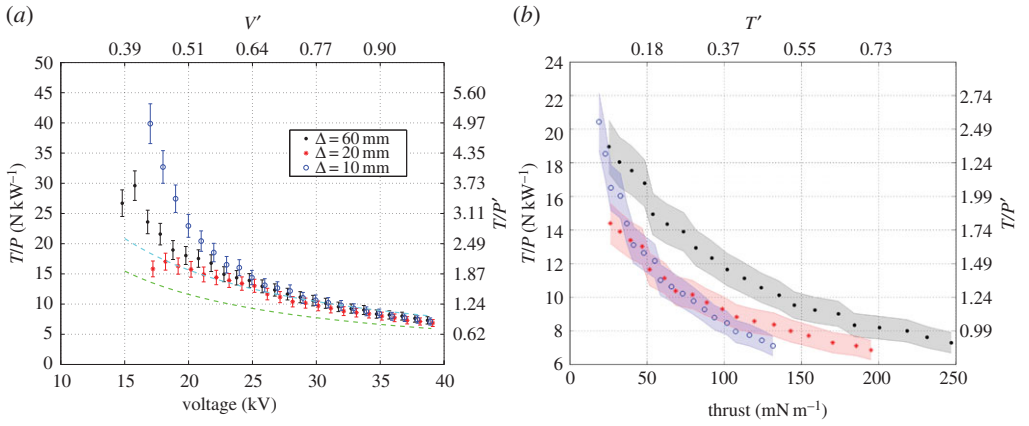

Figure 4. Thrust-to-power (T/P) data for the experimental data presented in figure 3: (*a*) T/P (N kW^{-1}) versus voltage (kV) and (*b*) T/P (N kW^{-1}) versus thrust (mN m^{-1}). Theoretical curves are plotted in (*a*) for dry (green, lower dashed line) and saturated (cyan, upper dashed line) air ion mobilities according to equation (2.2). Voltage offsets are given in (*a*) for readability. Uncertainty intervals are shaded in (*b*). (Online version in colour.)

which in turn determines the electric field shape. As stated in §2c, if variations in electrode geometry are small relative to the thrust-oriented gap distance between the electrodes, then the effect of electrode geometry on thrust-to-power is expected to be small. Deviations from 1D theory at voltages lower than approximately 25 kV are attributed to measurement bias not captured by the experimental uncertainty analysis. In particular, the sharp increase between the first two points for $\Delta = 60$ mm is the result of a non-proportional increase in thrust between 15 and 16 kV, yielding an increase in thrust-to-power ratio between those voltages.

When thrust-to-power ratio is plotted against thrust in figure 4*b*, the achieved T/P at a given thrust decreases with decreasing Δ above 50 mN m^{-1} ($T' = 0.18$). This follows from the observed reduction in current with respect to Δ at a given voltage from figure 4*a*; a higher voltage, and thus a higher power, is required to achieve a given current/thrust, thus reducing T/P. Figure 4*b* also highlights a potential trade-off between increasing thrust density—an increase in electrode pair packing density corresponds to a decreasing thrust-to-power ratio for a given thrust.

Finally, the spark breakdown voltage is not observed to decrease with pair spacing, as illustrated in figure 4*a*, where each configuration reached 39 kV without arcing. A possible explanation for the non-decreasing spark breakdown threshold with Δ follows from general 1D spark formation theory and the Meek criterion [21]; if pair interactions lead to decreased current at a given voltage, this implies reduced ionization at the emitting electrode. As the Meek criterion for streamer formation is directly dependent on this ionization rate, a higher voltage may be required to achieve spark breakdown. However, it is unknown if the arcing threshold increases as a function of pair spacing as applied potential limits based on anticipated sparking voltages were imposed for safety purposes. As a result, lower thrusts were observed for smaller Δ at the voltage limit, 39 kV.

(a) Thrust as a function of non-dimensional pair spacing

Figure 5 shows a non-dimensionalization of the relation between thrust and parallel pair spacing. The horizontal axis is the non-dimensional pair spacing, Δ/L. The vertical axis is the ratio between the thrust for a given configuration normalized by the thrust at the same electrode gap distance for $\Delta/L \approx 1$, or $T/T_{\Delta/L\approx1}$. Figure 5 shows that as Δ/L decreases through 1, the thrust ratio decreases. (Given the correlation between thrust and current, the same trend is observed in the current ratio, $I/I_{\Delta/L\approx1}$.) Above $\Delta/L = 1$, the thrust ratios asymptote to a value greater than 1, as suggested

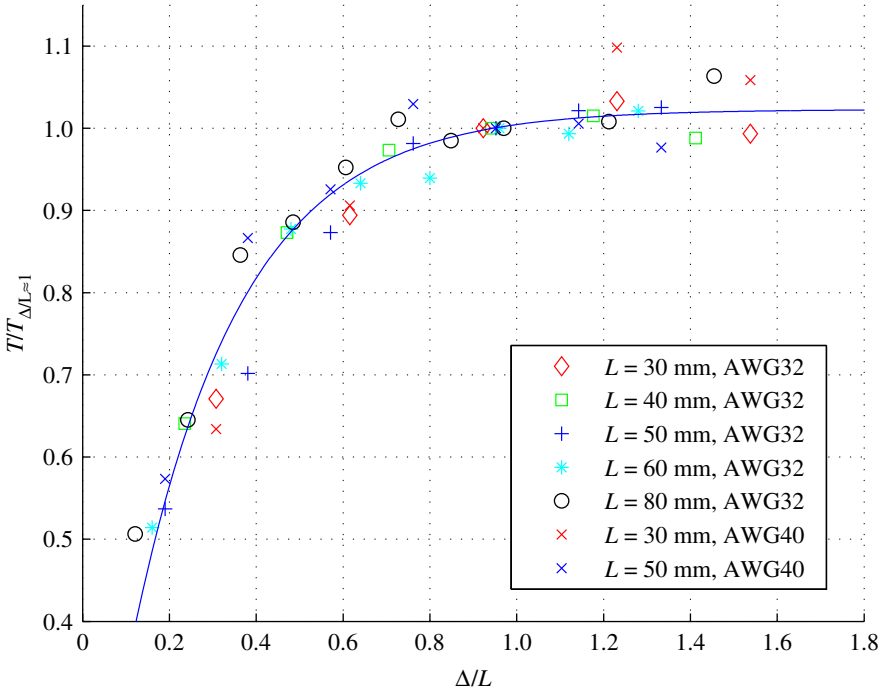

Figure 5. Non-dimensional thrust, $T/T_{\Delta/L\approx1}$, as a function of non-dimensional pair spacing, Δ/L, for different electrode gap distances and wire gauges. The blue line corresponds to the least-squares fit from equation (4.1). This fit has an r^2-value of 0.94. Uncertainty intervals are not shown for readability, but are approximately ±0.07 for each data point.

by the least-squares fit shown in blue. This implies that electric field interactions at these non-dimensional pair spacings are not sufficient to affect system performance. For the smallest Δ/L tested, the thrust ratio is approximately 0.51.

The dependence of thrust ratio on Δ/L is consistent across electrode gap distance as well as wire gauge, where no dependence on φ is indicated by the data. We note that figure 5 was generated by averaging thrust ratios over a range of voltages, each range being a function of L. The lower bound of this range is set by the voltage that induced at least a $0.1\,\mathrm{mA\,m^{-1}}$ current as to eliminate uncertainty at low thrust measurements. The upper bound of this range is set by the voltage at which spark breakdown or large current spikes owing to intermittent arcing were induced.

A consequence of figure 5 is that the thrust generated by this system is fundamentally limited by Δ/L regardless of the size of the thruster. The effect of pair interactions on the achievable thrust density of the EHD system is quantified in §5, but we begin the discussion here by considering the trend indicated in figure 5 and its possible influence on thrust density. The least-squares fit assumes a curve of the form $y = a(1 - \mathrm{e}^{bx})$, yielding

$$\frac{T}{T_{\Delta/L\approx1}} = 1.02 \cdot (1 - \mathrm{e}^{-4.0\cdot\Delta/L}). \tag{4.1}$$

Next, consider two alternative definitions of thrust per unit (frontal) area

$$\left(\frac{T}{A}\right)_1 = \frac{T_{\Delta/L,N}}{N \cdot \Delta \cdot s} \tag{4.2}$$

and

$$\left(\frac{T}{A}\right)_2 = \frac{T_{\Delta/L,N} - T_1}{(N-1) \cdot \Delta \cdot s} \tag{4.3}$$

where $T_{\Delta/L,N}$ is the thrust from a configuration with N electrode pairs with non-dimensional pair spacing Δ/L, T_1 is the thrust from a single electrode pair and s is the length of the emitting electrode. Equation (4.2) then defines the average thrust per unit area as the total system thrust divided by the total electrode pair working area, defined as $N \cdot \Delta \cdot s$. Equation (4.3), on the other hand, calculates the thrust contribution of $N-1$ additional pairs relative to the base case, T_1, and divides by the total additional working area, $(N-1) \cdot \Delta \cdot s$. In each case, thrust per unit area is estimated as a thrust divided by a characteristic area. However, $(T/A)_1$ does not consider changes in the marginal contribution of each pair as more pairs are considered.

To motivate these two different definitions further, assume that there is no increase in thrust with the addition of an arbitrary number of electrode pairs at a given Δ/L such that the numerator of equation (4.2) remains constant. Thus, the thrust density will tend to zero as the number of pairs goes to infinity but will be non-zero for finite N. Equation (4.3) yields a zero thrust density regardless of the value of N as no marginal contribution has been achieved though the addition of an electrode pair. While either quantity may be useful in characterizing a system, $(T/A)_1$ is potentially misleading as it is a quantity specific to the number of electrodes and may not scale with increasing N (e.g. doubling the number of electrodes, and thus doubling the working area does not double the system thrust). Given that the number of electrode pairs we can test is limited by the scale mass limit, a definition similar to $(T/A)_2$ in equation (4.3) will be used to calculate marginal thrust density in §§5 and 6 in order to estimate the behaviour in the limit of $N \to \infty$ with a finite number of pairs. One drawback of equation (4.3) is that it likely under-predicts the total thrust generated by a finite array of pairs by neglecting end effects.

If we now consider the two pair case ($N=2$), approximate the thrust for a given configuration using the thrust ratio from equation (4.1), assume that for $\Delta/L \gg 1$ the thrust from the two pair system is approximately twice that of the single pair system, and apply equation (2.1) such that $T_{\Delta/L\approx 1} = I_{\Delta/L\approx 1} L/\mu$, equation (4.3) becomes

$$\left(\frac{T}{A}\right)_2 = \frac{I_{\Delta/L\approx 1}}{\mu \cdot s}\frac{L}{\Delta}[0.51 - 1.02\mathrm{e}^{-4.0\cdot\Delta/L}]. \tag{4.4}$$

Equation (4.4) is maximized when $\Delta/L = 0.41$. This non-dimensional spacing corresponds to approximately 0.8 thrust ratio as predicted by equation (4.1). This result implies that thrust density is maximized when some interaction between electrode pairs is present, a result that is experimentally confirmed in §5a. Note that definition $(T/A)_2$ allows for negative thrust per unit area even when $T_{\Delta/L,N}$, the total system thrust, is greater than zero. In this component, negative thrust was not experimentally observed, indicating an additional drawback of defining thrust density by $(T/A)_2$. For this case, a negative estimated thrust density indicates a decrease in total thrust given an additional electrode pair, i.e. $T_{\Delta/L,N} < T_1$, not a net reverse thrust. However, a net reverse thrust is observed when staging is considered.

5. Component II results: thrust array

Figure 6*a* is a plot of the current ratio versus the number of parallel electrode pairs. The current ratio is defined as the current for a given configuration divided by the current of the configuration with the same electrode pair spacing, Δ, but where $N=2$. Thus the origin for each curve is (2,1). Figure 6*b* is a plot of an analogously defined thrust ratio versus the number of parallel electrode pairs. Both the current and thrust ratios are plotted for $L = 50$ mm and electrode pair spacings $\Delta = 10$ mm to 60 mm at an applied potential difference of 37 kV. While spark breakdown for $L = 50$ mm typically occurred at or near 40 kV, 37 kV was selected as it was the highest applied voltage where current oscillations induced by electrical arcing had not yet been observed.

As can be seen, when the non-dimensional pair spacing, Δ/L, is above the approximately identified threshold of 1, the current and thrust scale approximately with the number of electrode pairs. Ideally, with no pair interactions, the current and thrust ratio should scale exactly with the number of electrode pairs. Thus, we would expect the $N=5$ case to yield a 2.5

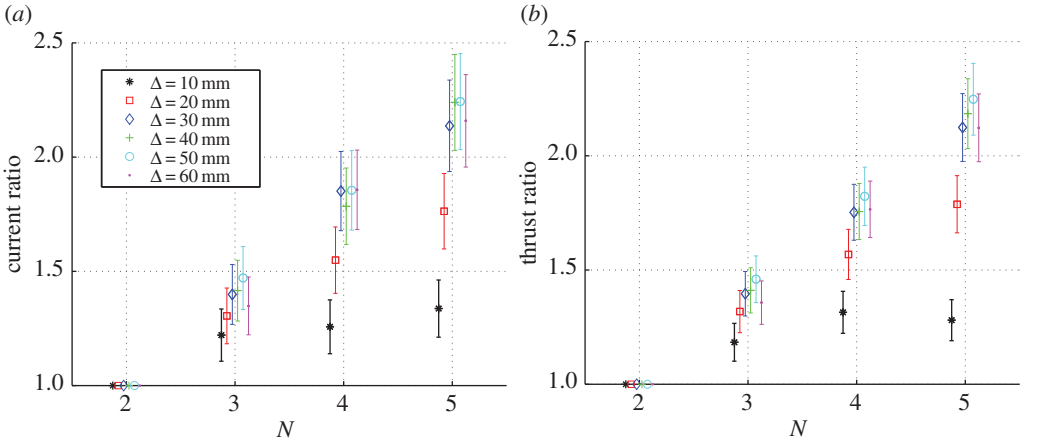

Figure 6. (*a*) Current and (*b*) thrust ratios versus the number of electrode pairs, N, for different electrode pair spacings, Δ. $L = 50$ mm and $\Delta V = 37$ kV. Offsets with respect to N are provided for readability. (Online version in colour.)

factor increase in current and thrust relative to the $N = 2$ case. Figure 6 shows that the actual factor increase in current is approximately 2.2, where the source of the discrepancy relative to the ideal case is unknown and is not captured by experimental uncertainty. The thrust ratios in figure 6*b* are approximately equal to their corresponding current ratios. For the $L = 30$ mm case (not plotted) an approximately 5% lower thrust ratio relative to the current ratio was consistently observed at voltages near spark breakdown relative to the current ratio. We attribute this behaviour to losses that cause deviation from the linear current/thrust scaling owing to the secondary discharge associated with performance degradation observed in figure 3*b* and discussed in §4. This secondary discharge is also a possible explanation for the surpassing of the current ratio as a function of N seen, for example in the case of $\Delta = 60$ mm between $N = 3$ and 4 in figure 6*a*. The observed increase in current ratio relative to the other plotted pair spacings is captured by the estimated experimental uncertainty and could be attributed to an earlier onset of this secondary discharge for the given voltage, thus raising the mean current per electrode pair.

As the electrode pair spacing decreases, there are corresponding decreases in both the current and the thrust ratios. For instance, figure 6 shows that between spacings of 60 mm and 10 mm, the current ratio decreases from approximately 2.2 to 1.3 when five electrode pairs are considered. This corresponds to a decrease of approximately 2.1–1.2 in the thrust ratio. Regardless of electrode pair spacing, the addition of an electrode pair yields an increase in both current and thrust for the considered pair spacings in all cases except for the $\Delta = 10$ mm, $N = 5$ case where a decrease in thrust ratio is observed. No such cases were observed for the $L = 30$ mm configurations, although the smallest Δ/L tested was 0.33 compared with 0.2 for the $L = 50$ mm case. This is captured by the estimated experimental uncertainty, as indicated by the plotted interval. The trends observed in figure 6 also hold for other applied voltages, although thrust measurement error distorts trends at low current occurring just after corona inception.

(a) Quantifying thrust density

As outlined in §4, we calculate thrust density on a marginal basis to estimate the thrust generated by an infinite array of electrode pairs with a finite number of tested pairs. We estimate thrust per unit area and thrust per unit volume as

$$\frac{T}{A} \approx \frac{T_{N>2,\Delta} - T_{N=2,\Delta}}{(N-2)\cdot\Delta\cdot s} \tag{5.1}$$

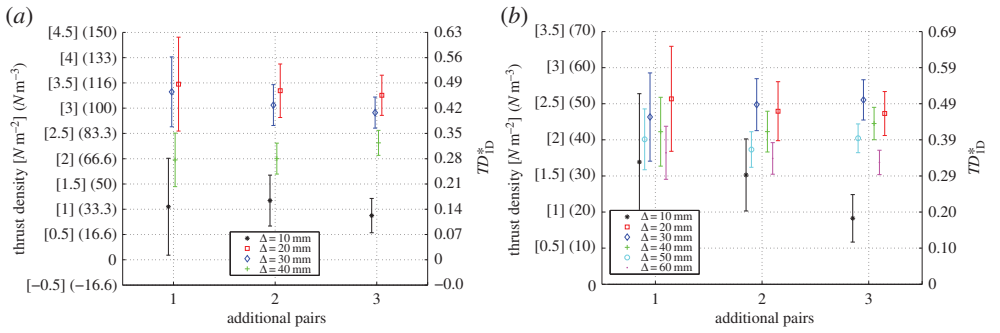

Figure 7. Estimated marginal thrust per unit area and volume (left axis) and normalized thrust density TD^*_{1D} (right axis) for different electrode pair spacings (*a*) $L = 30$ mm, $V = 28$ kV and (*b*) $L = 50$ mm, $V = 39$ kV. Offsets with respect to additional pairs are provided for readability. (Online version in colour.)

and

$$\frac{T}{\mathcal{V}} \approx \frac{T_{N>2,\Delta} - T_{N=2,\Delta}}{(N-2)\cdot\Delta\cdot L\cdot s}, \tag{5.2}$$

respectively, where $T_{N>2,\Delta}$ is the thrust of a configuration with $N > 2$ electrode pairs and electrode pair spacing Δ, $T_{N=2,\Delta}$ is the thrust of a configuration with the same electrode pair spacing Δ but with $N = 2$ electrode pairs, $\mathcal{V}$ is volume and the other symbols have their previously defined meanings. This means that the above definitions of thrust per unit area and volume are computed as the average marginal contribution of each additional electrode pair divided by the additional working area or volume relative to the corresponding $N = 2$ configuration.

Figure 7 shows the calculated marginal thrust per unit area and volume (left axis) and normalized thrust density, TD^*_{1D} (right axis) as a function additional electrode pairs, e.g. 1 denotes one additional electrode pair and thus three total pairs, and pair spacing for (a) $L = 30$ mm and (b) $L = 50$ mm. TD^*_{1D} is the thrust per unit area or volume normalized by the theoretical 1D maximum for a given L and voltage from equation (2.10). The data are plotted for a specified voltage for all electrode pair spacings considered. The voltages were selected as the highest for which data for all configurations were available for a given L. As the pair spacing is decreased through $\Delta/L = 1$, the marginal thrust density initially increases given that the working area/volume is decreasing at a faster rate than the associated decrease in thrust. At a critical spacing, the decrease in thrust dominates the decrease in working area, and an overall decrease in thrust density is calculated. For the case of $L = 30$ mm in figure 7*a*, a decrease in marginal thrust density is observed between pair spacings of 20 and 10 mm. This implies an optimal spacing between 10 and 30 mm, or $0.33 < \Delta/L < 1$. Similarly, for the case of $L = 50$ mm in figure 7*b*, a decrease in marginal thrust density is observed between pair spacings of 20 and 30 mm, indicating an optimal spacing between 20 and 40 mm, or $0.4 < \Delta/L < 0.8$. In both cases, the Δ/L bounds include the optimal non-dimensional spacing of 0.41 estimated by the analysis in §4a.

Maximum estimated marginal thrust densities from figure 7 calculated for three additional pairs are approximately 3.3 (2.9–3.7) N m^{-2} and 110 (97–120) N m^{-3} for $L = 30$ mm and 2.6 (2.3–2.8) N m^{-2} and 51 N m^{-3} (46–56) for $L = 50$ mm. Using equation (2.10), the theoretical maximum thrust per unit area (volume) for each gap distance is 7.1 N m^{-2} (237 N m^{-3}) and 5.1 N m^{-2} (103 N m^{-3}), respectively. These densities were computed assuming corona inception voltages recorded for the largest pair spacings tested. The estimated thrust densities correspond to achieving approximately 46 and 51% of the 1D theoretical maximum thrust densities in each case, as shown on the right axes. Variation is observed in the estimated thrust density as a function of the number of additional pairs, although in the majority of the cases, the estimated thrust densities appear to have converged and repeatability in thrust density estimates is indicated by the overlapping uncertainty intervals for a given pair spacing in figure 7. A case where this has not occurred is the $\Delta = 10$ mm, $L = 50$ mm configuration, where estimated thrust density decreases

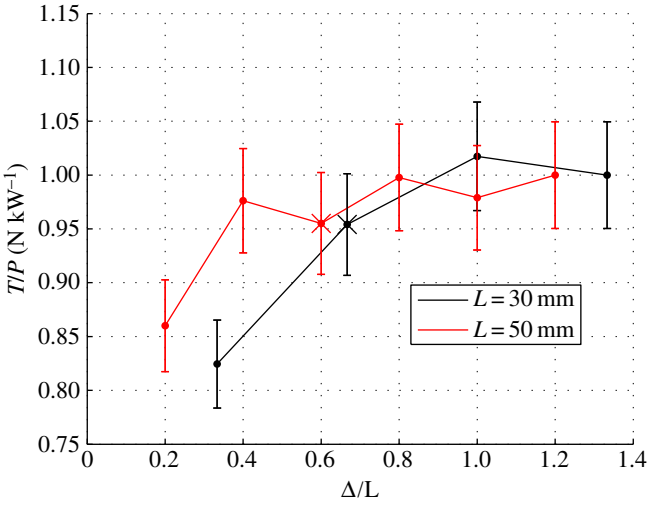

Figure 8. Normalized thrust-to-power ratio, T/P^*, plotted against non-dimensional pair spacing. Δ/L, for the same voltages as indicated in figure 7. Δ/L that maximizes thrust density has been indicated with a cross for each electrode gap distance.

by 46% between the first and the third additional pairs. In this case, the marginal contribution associated with each additional pair is decreasing as N is increased. At the pair spacings that yielded the highest thrust densities, variations between the first and third additional pairs are 7% and 10% for $L = 30$ mm and $L = 50$ mm, respectively.

The difference between experimentally estimated and 1D theoretical thrust densities is due to two factors. First, different electrode geometries may have different current density limits. For instance, a pair of concentric cylinder electrodes has a three times higher theoretical maximum current density than that determined by equation (2.7) for a given voltage and electrode gap distance. This derivation is briefly summarized in the electronic supplementary material. Second, as we have shown experimentally, electrode pair interactions limit the achievable thrust density. As a result, even if the theoretical maximum thrust per unit area of electrode were higher for the wire-to-cylinder geometry, the thrust density relative to the total working area is lower for this geometry as pair interaction losses are found to dominate. For our chosen geometry, the loss in thrust resulting from pair interactions yields a thrust per unit area approximately 50% lower than the predicted 1D maximum for both $L = 30$ and 50 mm. This does not imply that we have achieved 50% of the theoretical maximum, rather that the thruster studied here operates with a thrust per unit area approximately half that of an ideal 1D thruster. Different electrode geometries (e.g. pin-to-mesh) may yield different thrust densities relative to the 1D parallel plate theoretical maximum, and, in turn, have different fundamental thrust density limits.

Finally, our analysis has shown a decrease in the maximum achieved thrust density with an increase in electrode gap distance. Returning to the average electric field, V_a/L, the maximum experimentally observed average electric field magnitudes are 9.3×10^5 and 7.8×10^5 V m^{-1} for $L = 30$ mm and $L = 50$ mm, respectively. Thus, the decrease in estimated thrust densities also corresponds to a decrease in the theoretical maximum from equation (2.10). On average, it was observed that a 10 mm gap distance increase yielded an approximately 5 kV increase in the spark breakdown threshold. For the observed spark breakdown voltages and considering gap distances of 10 mm and above, this corresponds to a decrease in maximum V_a/L with increasing gap distance.

(b) Thrust-to-power considerations

Figure 8 plots T/P^* for both considered electrode gap distances versus non-dimensional pair spacing, Δ/L, for the same voltages used in generating figure 7, where T/P^* is the thrust-to-power

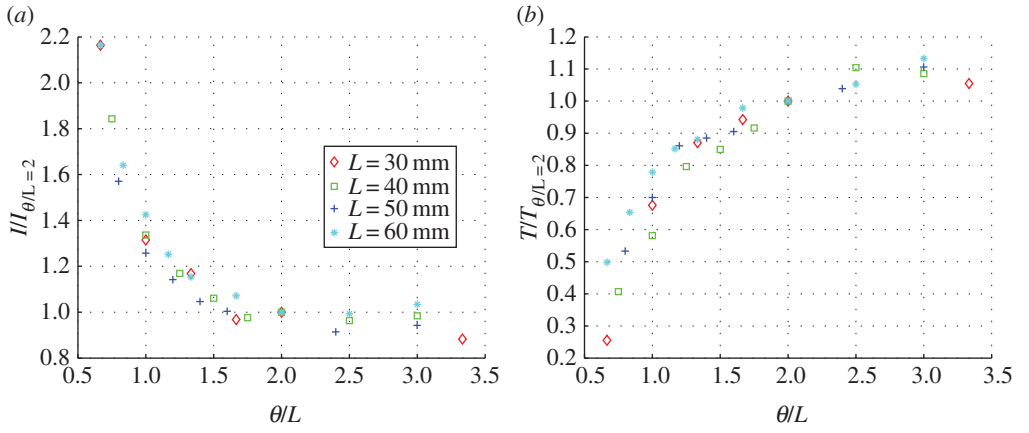

Figure 9. Non-dimensional (*a*) current, $I/I_{\theta/L} = 2$, and (*b*) thrust, $T/T_{\theta/L} = 2$, as a function of non-dimensional stage spacing, θ/L. Uncertainty intervals are not plotted for readability, but are approximately ± 0.1 in both (*a*) and (*b*). (Online version in colour.)

Table 1. Comparison of thrust-to-power ratios for different target levels of thrust per unit area. The Δ that maximize thrust per unit area for each value of L is assumed.

thrust per unit area (N m^{-2})	1	1.5	2	2.5
$L = 30$ mm	7.9	7.0	6.3	5.8
$L = 50$ mm	10.2	8.9	7.9	6.8

ratio for a given Δ/L normalized by T/P at the largest plotted Δ/L. In both cases, the smallest pair spacings, corresponding to non-dimensional spacings of 0.33 and 0.2 for $L = 30$ mm and $L = 50$ mm, respectively, yielded the lowest calculated thrust-to-power ratio. At the spacings for which thrust per unit area is maximized (indicated by a cross), thrust-to-power ratios are 4% lower. The gains in thrust density, on the other hand, are 40% and 55%. Although theory from §2c predicts no change in thrust-to-power ratio with increased pair density, figure 8 indicates a trade-off does exist for sufficiently high packing density. We hypothesize this trade-off, which is apparent at the smallest pair spacings, is due to system losses such as aerodynamic drag associated with electrodes which were not considered in the derivation from §2c.

Table 1 shows the achieved thrust-to-power ratios for different target levels of thrust per unit area achieved by both electrode gap distances. Ratios were estimated assuming the Δ that maximized thrust per unit area for each L. First, thrust-to-power ratios decrease with increasing thrust per unit area, which follows from the required increase in supplied power. Second, the thrust-to-power ratios are higher for the case of the longer electrode gap distance, although this difference in thrust-to-power ratio decreases from 23% to 15% for thrusts densities of 1 to 2.5 Nm^{-2}. While a higher maximum thrust per unit area is achieved for electrode pairs operating in parallel for $L = 30$ mm, more thrust is produced per unit power for $L = 50$ mm when comparing thrust densities achieved by both configurations.

6. Component III results: thrust staging

Figure 9 shows normalized thrust and current versus non-dimensional stage spacing, θ/L, where each stage consists of two electrode pairs with non-dimensional pair spacing $\Delta/L = 2$. Thrust and current are normalized by the data from the $\theta/L = 2$ configuration. We find that two trends emerge. First, as θ/L decreases, the overall thrust generated by the two stages decreases. Second,

as θ/L decreases, the overall induced current increases. For example, when $\theta/L = 1$, the thrust ratio has decreased to between 0.6 and 0.8, while the current ratio has increased to between 1.3 and 1.4. No dependence of the thrust and current ratios on L is apparent from figure 9, as was also in the case in §4a.

We hypothesize that these trends are due to the interactions between the collecting electrode of the first stage and the emitting electrode of the second stage. As the two stages are brought closer together, a discharge is induced between stages. This generates reverse ion flow, reducing net thrust, while also increasing current. Thus, the thrust-to-power ratio will decrease with θ/L. This hypothesis is supported by the observation of a net reverse thrust at the smallest stage spacings tested for each considered electrode gap distance. For example, a net reverse thrust is observed at spark breakdown for $\theta/L = 0.4$ when $L = 50$ mm. In addition, the breakdown voltage for this non-dimensional stage spacing is approximately half that of the $\theta/L > 1$ configurations given the smaller effective electrode gap distance between the stages.

(a) Quantifying thrust density

In order to calculate the achieved thrust per unit volume, a similar approach as used in §5a is applied. Here, we consider the marginal contribution of two factors: (1) the thrust gained by adding the second stage and (2) the thrust gained by adding an additional electrode pair to each stage. In order to reduce the overall number of tested configurations, contribution (2) is determined by considering the thrust generated by two versus three electrode pairs per stage. In addition, Δ is not varied and is selected to be 20 mm for $L = 30$ mm and 30 mm for $L = 50$ mm, each corresponding to the configurations that achieved the highest estimated thrust per unit area in §5a. Thus, we estimate thrust per unit volume by accounting for the marginal contribution of an additional electrode pair and an additional stage. For a given stage spacing and number of electrode pairs, the marginal thrust contribution of an additional stage is

$$\Delta T_{\mathrm{s}} = T_{\theta,N,K+1} - T_{\theta,N,K},$$

where $T_{\theta,N,K}$ is the thrust generated at stage spacing, θ, for N electrode pairs per stage and K stages. Similarly, for a given stage spacing and number of stages, the marginal thrust contribution of an additional pair is

$$\Delta T_{\mathrm{p}} = T_{\theta,N+1,K} - T_{\theta,N,K}.$$

It then follows that the marginal thrust contribution per stage, per pair is

$$\Delta T_{\mathrm{s,p}} = (T_{\theta,N+1,K+1} - T_{\theta,N+1,K}) - (T_{\theta,N,K+1} - T_{\theta,N,K}).$$

Dividing this quantity by the additional working volume and using the fact that three versus two pairs and two versus one stage were used to estimate thrust per unit volume in this component defines thrust per unit volume as

$$\frac{T}{\mathcal{V}} \approx \frac{(T_{\theta,N=3,K=2} - T_{\theta,N=3,K=1}) - (T_{\theta,N=2,K=2} - T_{\theta,N=2,K=1})}{(\theta + L) \cdot \Delta \cdot s}. \tag{6.1}$$

On the right-hand side of equation (6.1) the first term in parentheses in the numerator is the marginal contribution of the second stage when three electrode pairs per stage are considered, whereas the second term is the marginal contribution of the second stage when two electrode pairs are considered. Taking the difference of these two terms provides the marginal contribution of the third versus second electrode pair per stage. The marginal increase in volume given in the denominator is defined by the distance $\theta + L$ as it accounts for the increase in volume associated with both the additional electrode pair as well as the required spacing between stages.

Figure 10*a* presents the estimated thrust per unit volume as defined by equation (6.1), while figure 10*b* presents normalized thrust per unit volume relative to the theoretical 1D maximum. Data are shown for two different voltages for an electrode gap distance of 30 mm. We find that the highest thrust per unit volume is achieved for a stage spacing between 60 and 100 mm, or

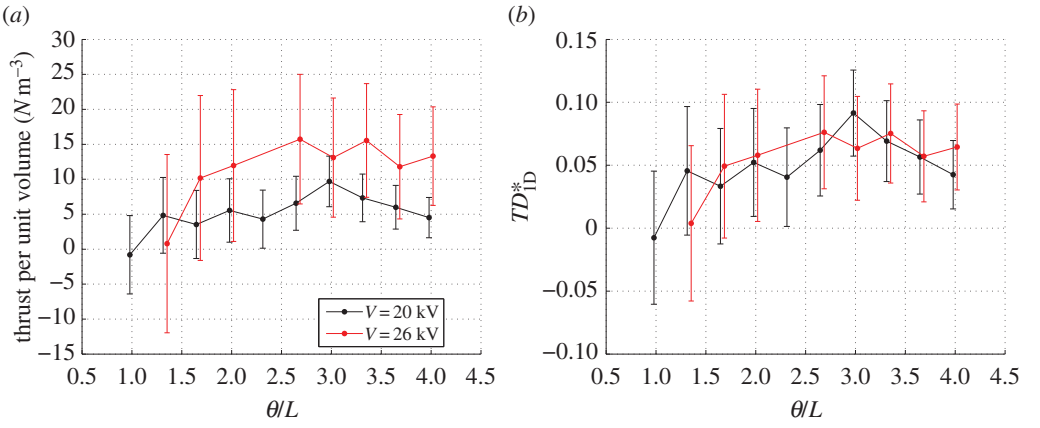

Figure 10. Marginal thrust per unit volume (*a*) plotted dimensionally (N m^{-3}) and (*b*) non-dimensionally for two voltages. $L = 30$ mm.

$2 < \theta/L < 3.3$. While uncertainty is on the order of the estimated thrust per unit volume, the mean trend appears to be the following: as voltage is increased, the peak thrust per unit volume also increases owing to the increase in current and thrust. As stage spacing, θ, continues to decrease, the thrust per unit volume decreases owing to the increasingly dominant thrust loss from stage interactions. At a stage spacing of approximately $\theta/L > 3$, the thrust per unit volume decreases given that the working volume considered increases, but thrust is approximately constant.

The maximum thrust per unit volume observed for $L = 30$ mm is approximately 15 N m^{-3}, with uncertainty intervals spanning from 6 to 25 N m^{-3}. This corresponds to approximately 13% of the experimentally estimated maximum thrust per unit volume from §5*a* and, as can be seen from figure 10*b*, 8% of the theoretical maximum value derived from equation (2.10). Our volume here includes 'dead space' between stages and so thrust density is expected to be lower than the single-stage estimates. The current and thrust data used in generating the thrust staging results are on average 20% lower than the data used in §5 for $L = 30$ mm, where the differences were noted in RH at the time of testing (68% versus 60%). Figure 10*b* shows that TD^*_{1D} is not shown to be a function of voltage, i.e. the thrust density normalized by the corresponding theoretical 1D maximum for a given voltage does not change as voltage increases. This behaviour is also observed for voltages not plotted in figure 10*b*.

For the case of $L = 50$ mm, similar trends are observed, but the maximum thrust per unit volume is approximately 5 N m^{-3}, a greater than 50% decrease in achievable thrust per unit volume relative to the $L = 30$ mm case. This decrease is due to the lower achieved thrust per unit area, as estimated previously in §5, as well as the larger working volume given the longer electrode gap distance and stage spacing.

(b) Thrust-to-power considerations

As can be directly inferred from figure 9, thrust-to-power ratio will decrease with decreasing θ/L and increasing voltage. Thus, although the maximum thrust per unit volume is realized at a θ/L between 2 and 3.3, the thrust-to-power ratio is monotonically decreasing with decreasing θ/L, indicating a trade-off between maximizing thrust per unit volume and maximizing T/P. Note that because not all current tubes begin and end on the same electrodes owing to interactions between stages, the results from §2c are not applicable, and thrust-to-power ratio is expected to decrease with stage spacing. Table 2 provides a comparison of observed thrust-to-power ratios for different target levels of thrust per unit volume achieved by the two-stage thruster. For the four values of thrust per unit volume considered, thrust-to-power ratio is higher for the smaller electrode gap distance, although this difference is observed to decrease from approximately

Table 2. Comparison of thrust-to-power ratios (N kW^{-1}) for different target levels of thrust per unit volume.

thrust per unit volume (N m^{-3})	4	5	6	7
$L = 30$ mm	8.3	7.4	6.8	6.4
$L = 50$ mm	6.9	6.6	6.3	5.9

19% to approximately 7% with increasing thrust density. So, while table 1 showed that higher thrust-to-power ratio was achieved for $L = 50$ mm when comparing thrust per unit area, higher thrust-to-power is now observed for $L = 30$ mm when comparing thrust per unit volume and considering stage interactions.

7. Conclusion

Previous analysis has quantified EHD thruster performance. Specifically, Masuyama & Barrett [23] reported thrust-to-power ratios on the order of 10 N kW^{-1} and as high as 100 N kW^{-1} as compared with approximately 2 N kW^{-1} for jet propulsion. While potentially competitive with conventional propulsion in this respect, it was previously unknown if EHD could produce a thrust density that is potentially useful for aircraft propulsion. The purpose of this analysis was to quantify the achievable thrust density from EHD propulsion for a wire-to-cylinder electrode geometry. This was done by considering variations in different geometric parameters relating distances between electrode pairs for both parallel and series operation.

We found that that as two electrode pairs operating in parallel and series are brought closer together, the current and thrust characteristics of the system are affected. In particular, parallel electrode pairs see decreases in both current and thrust as the spacing between the electrodes is decreased, where the thrust ratio has decreased to between 0.8 and 0.9 for a non-dimensional pair spacing of approximately 0.5. In the case of series electrode pairs, a decrease in thrust is also observed when the distance between stages is decreased, but a higher current is induced. The thrust ratio has decreased to approximately 0.7 for a non-dimensional stage spacing of 1, whereas the current ratio has increased to approximately 1.3.

Thrust densities were computed for both parallel and series operation. When considering electrode pairs operating in parallel, only, thrusts per unit area of 3.3 N m^{-2} and 2.6 N m^{-2} were achieved for gap distances of 30 mm and 50 mm, respectively. Both of these densities were less than the theoretical 1D maximum thrust per unit area identified by equation (2.10), where equation (2.10) was derived through an extension of the Mott–Gurney law that considered a non-choked solution. These thrusts per unit area corresponded to thrusts per unit volume of 110 and 50 N m^{-3}. When also considering series operation, estimated thrusts per unit volume decreased to approximately 15 N m^{-3} for a 30 mm gap distance and to approximately 5 N m^{-3} for a 50 mm gap distance. Given the observed trends from this analysis, we expect that higher thrust densities may be possible with shorter electrode gap distances.

A vehicle that uses EHD propulsion will likely have the propulsive mechanism encompass the entire body of the aircraft. As a result, a potential EHD aircraft and a conventional aircraft are not directly comparable on the basis of thrust density given that, for example, turbofan engines produce thrust on the order of 10 000 N m^{-2}. In order to provide context on whether the thrust densities estimated in this study are of potentially sufficient magnitude for in-atmosphere propulsion applications, we compare these values to characteristic thrust densities derived for aircraft with conventional propulsion systems. These characteristic thrust densities are calculated by first defining a characteristic volume for the aircraft based on fuselage height/width, wingspan and length, then determining the rated engine output and/or aerodynamic characteristics of the aircraft, and finally using this information to calculate a characteristic thrust per unit area and volume.

Table 3 provides a summary of characteristic thrust densities for three different aircraft. The 'MIT Fast A' and 'MIT Fast B' are classified as small unmanned aerial vehicles (UAVs) (T Tao,

Table 3. Estimated characteristic thrust densities for three example aircraft: the 'MIT Fast A', 'MIT Fast B' (T Tao 22 April 2014, personal communication) and the A320 (http://www.airbus.com/aircraftfamilies/passengeraircraft/a320family/a320/specifications/).

aircraft	MIT fast A	MIT fast B	Airbus A320
T/A (N m^{-2})	5.2	6.8	1180
$T/\mathcal{V}$ (N m^{-3})	3.0	6.1	31.5

22 April 2014, personal communication), while the A320 is a commercial jet aircraft with a maximum range of approximately 6100 km. For the case of the UAVs, while the thrust per unit area is a factor of 1.6–2.1 higher than the maximum parallel thrust density observed experimentally in this analysis, the characteristic thrust per unit volume is included in the range of estimated thrusts per unit volume. For the case of the A320, the characteristic thrust per unit area is three orders of magnitude larger than that achieved in this analysis, while the characteristic thrust per unit volume is two to three times larger than that measured with EHD in this study. Our experimental results of thrust densities up to approximately 10 N m^{-3} suggest that EHD propulsion has most likely potential feasibility at the small UAV scale. However, we note that the theoretical maximum volumetric thrust density computed using our extended Mott–Gurney law is an order of magnitude higher.

We also identified trade-offs inherent in EHD propulsion systems. As previously observed by Masuyama & Barrett [23], for a given electrode gap distance, thrust-to-power ratio decrease with increasing power and thrust, as indicated by equation (2.2). A similar trade-off exists between thrust density and thrust-to-power ratio—increasing thrust density comes at the cost of decreasing the thrust-to-power ratio, where thrust density can be increased by increasing the power supplied to a given configuration or by decreasing the working volume through decreases in pair or stage spacing. The former leads to a decrease in thrust-to-power ratio as indicated by equation (2.2). The latter leads to a decrease in thrust-to-power ratio given increased pair and stage interactions that alter the current–voltage relationship and increase the required power required for a given thrust.

When considering parallel operation for the configurations that yielded the highest estimated thrust densities, the longer gap distance generated higher thrust-to-power ratios for a given thrust per unit area, although the maximum thrust density achieved by the longer electrode pair configurations was lower than that achieved by the shorter electrode pair configurations. This suggests an additional trade-off between the range of achievable thrusts per unit area and the associated thrust-to-power ratio, i.e. increased operational flexibility implies lower thrust-to-power ratio. When multiple stages were considered, we found that shorter electrode gap distances for the same target thrust per unit volume yielded on average higher thrust-to-power ratios. In addition, a higher maximum thrust per unit volume was also calculated for the shorter gap distance. This suggests a benefit in using shorter electrode gap distances to maximize both thrust per unit volume and achieved thrust-to-power ratio when considering multiple stage thrusters.

Data accessibility. There are no datasets associated with this paper.

Acknowledgements. The authors thank Joseph Salinas for his help with the experimental set-up and Isaac Lajoie, Will Rutter and Adam Sanders for their help in generating experimental results.

Author contributions. C.K.G. and S.B. designed the research and wrote the paper. C.K. carried out the experiments.

Funding statement. The authors thank the Martin Family Society for Fellows for Sustainability for helping to fund this work.

Conflict of interests. The authors have no competing interests.

References

1. Robinson M. 1961 Movement of air in the electric wind of the corona discharge. *AIEE Trans.* **80**, 143–150.

2. Owsenek BL, Seyed-Yagoobi J. 1997 Theoretical and experimental study of electrohydrodynamic heat transfer enhancement through wire-plate corona discharge. *J. Heat Transfer* **119**, 604–610. (doi:10.1115/1.2824148)
3. Allen PHG, Karayiannis TG. 1995 Electrohydrodynamic enhancement of heat transfer and fluid flow. *Heat Recovery Syst. CHP* **15**, 389–423. (doi:10.1016/0890-4332(95)90050-0)
4. Laohalertdecha S, Naphon P, Wongwises S. 2007 A review of electrohydrodynamic enhancement of heat transfer. *Renew. Sustain. Energy Rev.* **11**, 858–876. (doi:10.1016/j.rser.2005.07.002)
5. Yamamoto T, Velkoff HR. 1981 Electrohydrodynamics in an electrostatic precipitator. *J. Fluid Mech.* **108**, 1–18. (doi:10.1017/S002211208100195X)
6. Zhao L, Adamiak K. 2005 EHD flow in air produced by electric corona discharge in pin–plate configuration. *J. Electrost.* **63**, 337–350. (doi:10.1016/j.elstat.2004.06.003)
7. Hohman MM, Shin M, Rutledge G, Brenner MP. 2001 Electrospinning and electrically forced jets. I. Stability theory. *Phys. Fluids* **13**, 2201–2220. (doi:10.1063/1.1383791)
8. Shin YM, Hohman MM, Brenner MP, Rutledge GC. 2001 Experimental characterization of electrospinning: the electrically forced jet and instabilities. *Polymer* **42**, 09 955–09 967. (doi:10.1016/S0032-3861(01)00540-7)
9. Stuetzer OM. 1960 Ion drag pumps. *J. Appl. Phys.* **31**, 136–146. (doi:10.1063/1.1735388)
10. Pickard WF. 1963 Ion drag pumping. I. Theory. *J. Appl. Phys.* **34**, 246–250. (doi:10.1063/1.1702592)
11. Seyed-Yagoobi J. 2005 Electrohydrodynamic pumping of dielectric liquids. *J. Electrost.* **63**, 861–869. (doi:10.1016/j.elstat.2005.03.047)
12. Zhao L, Adamiak K. 2005 Numerical analysis of forces in an electrostatic levitation unit. *J. Electrost.* **63**, 729–734. (doi:10.1016/j.elstat.2005.03.036)
13. Martins AA, Pinheiro MJ. 2011 Modeling of an EHD corona flow in nitrogen gas using an asymmetric capacitor for propulsion. *J. Electrost.* **69**, 133–138. (doi:10.1016/j.elstat.2011.02.002)
14. Martins AA, Pinheiro MJ. 2011 On the influence that the ground electrode diameter has in the propulsion efficiency of an asymmetric capacitor in nitrogen gas. *Phys. Plasmas* **18**, 033512. (doi:10.1063/1.3562874)
15. Martins AA. 2013 Modelling of an improved positive corona thruster and actuator. *J. Electrost.* **71**, 61–67. (doi:10.1016/j.elstat.2012.09.001)
16. Adamiak K. 2013 Numerical models in simulating wire-plate electrostatic precipitators: a review. *J. Electrost.* **71**, 673–680. (doi:10.1016/j.elstat.2013.03.001)
17. Davis JL, Hoburg JF. 1983 Wire-duct precipitator field and charge computation using finite element and characteristics methods. *J. Electrost.* **14**, 187–199. (doi:10.1016/0304-3886(83)90006-2)
18. Roth JR, Sherman DM, Wilkinson SP. 2000 Electrohydrodynamic flow control with a glow-discharge surface plasma. *AIAA J.* **38**, 1166–1172. (doi:10.2514/2.1110)
19. Thomas FO, Corke TC, Iqbal M, Kozlov A, Schatzman D. 2009 Optimization of dielectric barrier discharge plasma actuators for active aerodynamic flow control. *AIAA J.* **47**, 2169–2178. (doi:10.2514/1.41588)
20. Braun EM, Lu FK, Wilson DR. 2008 A critical review of electric and electromagnetic flow control research applied to aerodynamics. In *Proc. 39th Plasmadynamics and Laser Conf., Seattle, WA, 23–26 June*. Red Hook, NY: Curran Associates, Inc.
21. Fridman A, Kennedy LA. 2004 *Plasma physics and engineering*. New York, NY: Taylor & Francis.
22. Christenson EA, Moller PS. 1967 Ion-neutral propulsion in atmospheric media. *AIAA J.* **5**, 1768–1773. (doi:10.2514/3.4302)
23. Masuyama K, Barrett SRH. 2013 On the performance of electrohydrodynamic propulsion. *Proc. R. Soc. A* **469**, 20120623. (doi:10.1098/rspa.2012.0623)
24. ICAO Aircraft Engine Emissions Databank. See http://easa.europa.eu/document-library/icao-aircraft-engine-emissions-databank.
25. Moreau E, Benard N, Lan-Sun-Luk JD, Chabriat JP. 2013 Electrohydrodynamic force produced by a wire-to-cylinder dc corona discharge in air at atmospheric pressure. *J. Phys. D* **46**, 475204. (doi:10.1088/0022-3727/46/47/475204)
26. Kiousis KN, Moronis AX, Fruh WG. 2014 Electro-hydrodynamic (EHD) thrust analysis in wire-cylinder electrode arrangement. *Plasma Sci. Technol.* **16**, 363. (doi:10.1088/1009-0630/16/4/11)

27. Colas DF, Ferret A, Pai DZ, Lacoste DA, Laux CO. 2010 Ionic wind generation by a wire-cylinder-plate corona discharge in air at atmospheric pressure. *J. Appl. Phys.* **108**, 103306. (doi:10.1063/1.3514131)
28. Saenz-Otero A, Pina A, Wellman G, Lozano P, Garriott R. 2010 Electrostatic thrusters for microgravity propulsion in a pressurized environment. In *IEEE Aerospace Conf.*, Big Sky, MT, 6–13 March, pp. 1–15. Red Hook, NY: Curran Associates, Inc.
29. Kaptsov NA. 1947 *Elektricheskie yavleniya v gazakh i vakuume*. Moscow, Russia: OGIZ.
30. Feng JQ. 1999 Application of Galerkin finite-element method with Newton iterations in computing steady-state solutions of unipolar charge currents in corona devices. *J. Comput. Phys.* **151**, 969–989. (doi:10.1006/jcph.1999.6229)
31. Tirumala R, Go DB. 2014 Comparative study of corona discharge simulation techniques for electrode configurations inducing non-uniform electric fields. *J. Electrost.* **72**, 99–106. (doi:10.1016/j.elstat.2013.12.003)
32. Rickard M, Dunn-Rankin D, Weinberg F, Carleton F. 2005 Characterization of ionic wind velocity. *J. Electrost.* **63**, 711–716. (doi:10.1016/j.elstat.2005.03.033)
33. Rickard M, Dunn-Rankin D, Weinberg F, Carleton F. 2006 Maximizing ion-driven gas flows. *J. Electrost.* **64**, 368–376. (doi:10.1016/j.elstat.2005.09.005)
34. Kim C, Park D, Noh KC, Hwang J. 2010 Velocity and energy conversion efficiency characteristics of ionic wind generator in a multistage configuration. *J. Electrost.* **68**, 36–41. (doi:10.1016/j.elstat.2009.09.001)
35. Tyndall AM, Grindley GC. 1926 The mobility of ions in air. Part I. Negative ions in moist air. *Proc. R. Soc. Lond. A* **110**, 341–364. (doi:10.1098/rspa.1926.0019)
36. Goebel DM, Katz I. 2008 *Fundamentals of electric propulsion: ion and Hall thrusters*. Hoboken, NJ: John Wiley & Sons.
37. Pekker L, Young M. 2011 Model of ideal electrohydrodynamic thruster. *J. Propul. Power* **27**, 786–792. (doi:10.2514/1.B34097)
38. Mott NF, Gurney RW. 1948 *Electronic processes in ionic crystals*. Oxford, UK: Clarendon Press.
39. Peek FW. 1920 *Dielectric phenomena in high voltage engineering*. New York, NY: McGraw-Hill Book Company, Incorporated.
40. Zahn M, Tsang CF, Pao SC. 1974 Transient electric field and space-charge behavior for unipolar ion conduction. *J. Appl. Phys.* **45**, 2432–2440. (doi:10.1063/1.1663610)
41. Sigmond RS. 1982 Simple approximate treatment of unipolar space-charge-dominated coronas: the Warburg law and the saturation current. *J. Appl. Phys.* **53**, 891–898. (doi:10.1063/1.330557)
42. Coleman HW, Steele WG. 2009 *Experimentation, validation, and uncertainty analysis for engineers*. Hoboken, NJ: John Wiley & Sons.
43. Ryzko H. 1965 Drift velocity of electrons and ions in dry and humid air and in water vapour. *Proc. Phys. Soc.* **85**, 1283–1295. (doi:10.1088/0370-1328/85/6/327)